Available online at www.sciencedirect.com
SciVerse ScienceDirect
Acta Materialia 60 (2012) 3128–3139
Acta MATERIALIA
www.elsevier.com/locate/actamat

Microstructural tailoring and improvement of mechanical properties in CuZr-based bulk metallic glass composites

Zengqian Liu [a], Ran Li [a,*], Gang Liu [b], Wenhuang Su [a], Hui Wang [a], Yan Li [a], Minjie Shi [a], Xuekun Luo [a], Guojuan Wu [a], Tao Zhang [a,*]

[a] *Key Laboratory of Aerospace Materials and Performance (Ministry of Education), School of Materials Science and Engineering, Beihang University, Beijing 100191, People's Republic of China*

[b] *State Key Laboratory for Mechanical Behavior of Materials, School of Materials Science and Engineering, Xi'an Jiaotong University, Xi'an 710049, People's Republic of China*

Received 27 September 2011; received in revised form 8 February 2012; accepted 10 February 2012
Available online 10 March 2012

Abstract

A strategy for homogenizing the B2 CuZr phase in CuZr-based bulk metallic glass (BMG) composites based on inoculation is presented. The sizes and distribution of B2 CuZr particles can be effectively homogenized by Ta additions in rapidly solidified $Cu_{47}Zr_{48-x}Al_5Ta_x$ ($0 \leqslant x \leqslant 1$, at.%) alloys. Mechanisms of the homogenizing effect were investigated by analyzing the microstructures of the composites as well as the nucleation and growth processes of the B2 CuZr phase. Mechanical properties of the alloys were significantly improved by the uniform B2 CuZr particles under both compression and tension. The inhibition on the propagation of shear bands and cracks by the ductile crystals and deformation-induced martensitic transformation of the B2 phase was proved to account for the superior tensile properties. Fracture mechanisms were proposed to correlate the tensile fracture behaviors to microstructural features of the alloys. Furthermore, the tensile plastic strain was quantitatively modeled by using the empirical microstructural element body approach as well as percolation theory. This study has important implications for the development and structural applications of high-performance BMG composites.

Keywords: Bulk metallic glass; Composites; Microstructures; Mechanical properties; Modeling

1. Introduction

As an important promising engineering material, bulk metallic glasses (BMGs) have attracted great attention owing to their unique properties compared with traditional crystalline alloys, such as high strength and large elastic strain limit [1–3]. However, their structural applications are strictly limited by the low ductility and macroscopic strain-softening nature at ambient temperature, especially under tensile conditions [4–7]. To overcome this brittleness, BMG composites with a crystalline phase at different length scales distributed within the glassy matrix have been fabricated by different methods in various glass-forming systems [8–17]. The toughness and ductility can be significantly improved even under tension in some BMG composites with properly adjusted compositions and microstructures [9,15,17]. Nevertheless, the macroscopic strain-softening behavior is still obvious in tension for these composites [18]. Recently, this drawback was successfully circumvented in some CuZr-based BMG composites reinforced by a shape memory B2 CuZr phase–shape memory BMG composites [18–22]. The composites exhibit distinct transformation-mediated work-hardening behavior and tensile ductility, which originate mainly from the deformation-induced reversible martensitic transformation of B2 CuZr to a monoclinic B19′ phase [18–23]. The

* Corresponding authors. Tel.: +86 10 82316192; fax: +86 10 82339705.
E-mail addresses: liran@buaa.edu.cn (R. Li), zhangtao@buaa.edu.cn (T. Zhang).

1359-6454/$36.00 © 2012 Acta Materialia Inc. Published by Elsevier Ltd. All rights reserved.
doi:10.1016/j.actamat.2012.02.017

pronounced mechanical properties make them more promising and attractive for practical applications as advanced structural materials.

Since the mechanical properties of these types of BMG composites depend strongly on their microstructures, an effective adjustment of the microstructure is essential for obtaining the desired combination of mechanical properties in the composites, including strength, ductility and work-hardening ability [22–34]. On the one hand, the volume fraction of the B2 CuZr phase can be roughly controlled by varying the cooling rate, which is normally achieved via changing sizes of cast samples [22,24,27,28,35–39]. Generally, the larger the cast sample size (i.e. the lower the cooling rate), the higher the volume fraction of the B2 CuZr phase in the composites. Owing to the thermodynamically unstable nature of this phase at temperatures below ~988 K, the cooling rate should be higher than a threshold value to prevent its eutectoid decomposition to low-temperature $Cu_{10}Zr_7$ and $CuZr_2$ equilibrium phases [40]. In addition, an upper critical cooling rate exists if one wishes to obtain the composite structure rather than the fully amorphous phase. Therefore, the cooling rate should be adjusted suitably over a moderate range in order to control the crystalline volume fraction in the composites. On the other hand, it has been verified that a homogeneous distribution of the B2 CuZr phase in the glassy matrix is beneficial for the mechanical properties of shape memory BMG composites [22,28,29]. However, the sizes and distribution of micron-scale crystalline particles are usually non-uniform because of the large temperature gradient and varying cooling rates across the samples as well as the "Soret effect" in the casting process [22–29,41,42]. It has been reported that the B2 CuZr phase precipitates not only in the center but also at the edge of the cast samples and tends to form a patch-like framework as the volume fraction increases, which results in a deterioration of the mechanical properties of the composites [22,29]. To homogenize the sizes and distribution of the shape memory phase, it is necessary to control the nucleation and growth of the crystalline particles from the unstable undercooled alloy melts during the rapid cooling process [18]. This is quite challenging because of the short time window for the operational treatment and the high sensitivity of the primary precipitate phase on the compositions as well as casting conditions [38,43,44]. Furthermore, the quantitative relationships between the microstructures and mechanical properties are always a matter of utmost importance for engineering alloys. Regarding BMGs and their composites, tensile plastic deformation is critical when related to the microstructural features. The study of quantitative relationships between microstructures and mechanical properties in tensile conditions has important implications for the development of high-performance BMG composites and their structural applications.

In this study, we present a strategy for homogenizing the sizes and distribution of B2 CuZr particles in shape memory BMG composites based on inoculation, an approach that is widely used in the grain refinement of traditional crystalline alloys [45]. Origins of the homogenizing effect were investigated by analyzing the nucleation and growth processes of the second phase. Mechanical properties as well as related deformation and fracture mechanisms of the composites were also analyzed and presented. The tensile ductility was further quantitatively correlated with the microstructures of the alloys using different modeling approaches.

2. Experimental

Master alloys with nominal compositions of $Cu_{47}Zr_{48-x}Al_5Ta_x$ ($0 \leqslant x \leqslant 1$, at.%) were prepared by arc-melting mixtures of constituent elements (purity > 99.9%) under Ti-gettered high-purity argon atmosphere. To ensure chemical homogeneity, Ta and Zr, which have relatively high melting points and large solid solubility at high temperatures, were arc-melted to form a pre-alloy before being remelted four times with Cu and Al [40]. The ingots were then remelted in a quartz tube by induction heating followed by injection into copper molds with cylindrical cavities in diameters ranging from 1 to 3 mm. Structures of the as-cast rods were analyzed by X-ray diffraction (XRD) using a Bruker AXS D8 X-ray diffractometer with a Cu target (Cu Kα, $\lambda = 0.1541$ nm), scanning electron microscopy (SEM, Hitachi S-530) and electron probe microanalysis (JEOL JXA 8100). Transmission electron microscopy (TEM) analysis was conducted on a JEM-2100F instrument equipped with a field emission gun. The samples for TEM investigation were thinned manually and then twin-jet electropolished using HNO_3:CH_4O = 1:3 solution at temperatures below −20 °C. Uniaxial compression tests were performed on 3 mm diameter samples with an aspect ratio of 2:1 at a strain rate of $2.08 \times 10^{-4}\ s^{-1}$ at room temperature. Tensile tests were also carried out at a strain rate of $3 \times 10^{-4}\ s^{-1}$ on samples with a gauge dimension of 1.5 mm diameter × 6 mm machined and polished from the 3 mm diameter rods. Fractography observations and microstructural examinations were conducted by SEM on a CamScan 3400 microscope.

3. Results

3.1. Microstructural evolution with Ta addition

Fig. 1 shows XRD patterns of the as-cast 3 mm diameter rods of the alloys with different Ta additions. The ternary $Cu_{47}Zr_{48}Al_5$ alloy without Ta addition exhibits a distinct diffraction pattern typical of the BMG composites—crystalline peaks identified as the B2 CuZr phase superimposed on a broad halo of amorphous matrix [21–32]. The crystalline peaks become nearly indistinctive for the alloy with 0.25% Ta addition and cannot be distinguished for the 0.5% Ta-added sample, indicating an improved glass-forming ability (GFA) for the alloys with

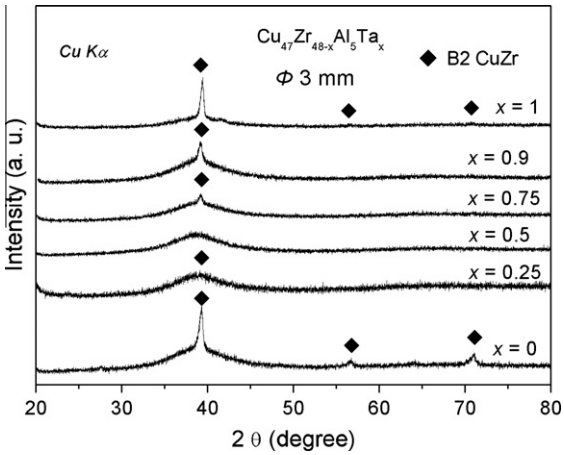

Fig. 1. XRD patterns of the 3 mm diameter rods of the alloys with different Ta additions.

Ta additions up to 0.5%. With further Ta additions, the B2 CuZr phase reprecipitates in the glassy matrix and exhibits increased volume fractions manifested by the improved relative intensity of crystalline peaks on the amorphous hump. For the 1% Ta-added sample, however, the crystalline phase is dominant judging from its strong crystalline peaks. Therefore, BMG composites with B2 CuZr precipitates can be obtained by properly adjusting the Ta contents of 0–0.5% or 0.5–1% under the present cooling rate and the alloy with 0.5% Ta addition shows the best GFA.

Fig. 2 presents SEM images of the cross-sections of the samples. A large volume fraction (~40%) of the B2 CuZr phase with heterogeneous distribution and non-uniform particle sizes is embedded in the glassy matrix for the Ta-free sample (Fig. 2a). The particles precipitate not only from the center of the rod where the cooling rate is lower but also at the surface contacting with the copper mold. Although the small particles are mostly spherical in shape, the larger ones show various morphologies and tend to impinge upon each other to form patch-like framework. Dendrite substructure is visible in the center of large particles but cannot be resolved by SEM in small ones, as shown in Fig. 3a. The above structural features are typically consistent with those reported for the composites in the Cu–Zr–Al system [22,25,29]. For the sample with 0.25% Ta addition, although only limited numbers of B2 CuZr particles can be found across the whole section, the surface of the rod is still confirmed to be a preferential site for the nucleation of the crystalline phase as indicated by the arrow (Fig. 2b). The 0.5% Ta-added sample displays a featureless morphology characteristic of BMGs which agrees well with the XRD results, confirming its amorphous nature (Fig. 2c).

With further increase in Ta contents, the B2 CuZr phase reappears in the samples but exhibits unique morphology and distribution features different from those previously mentioned. Spherical particles in uniform sizes from ~50 to ~180 μm are distributed homogeneously in the glassy matrix, as shown in Fig. 3b. The crystalline volume

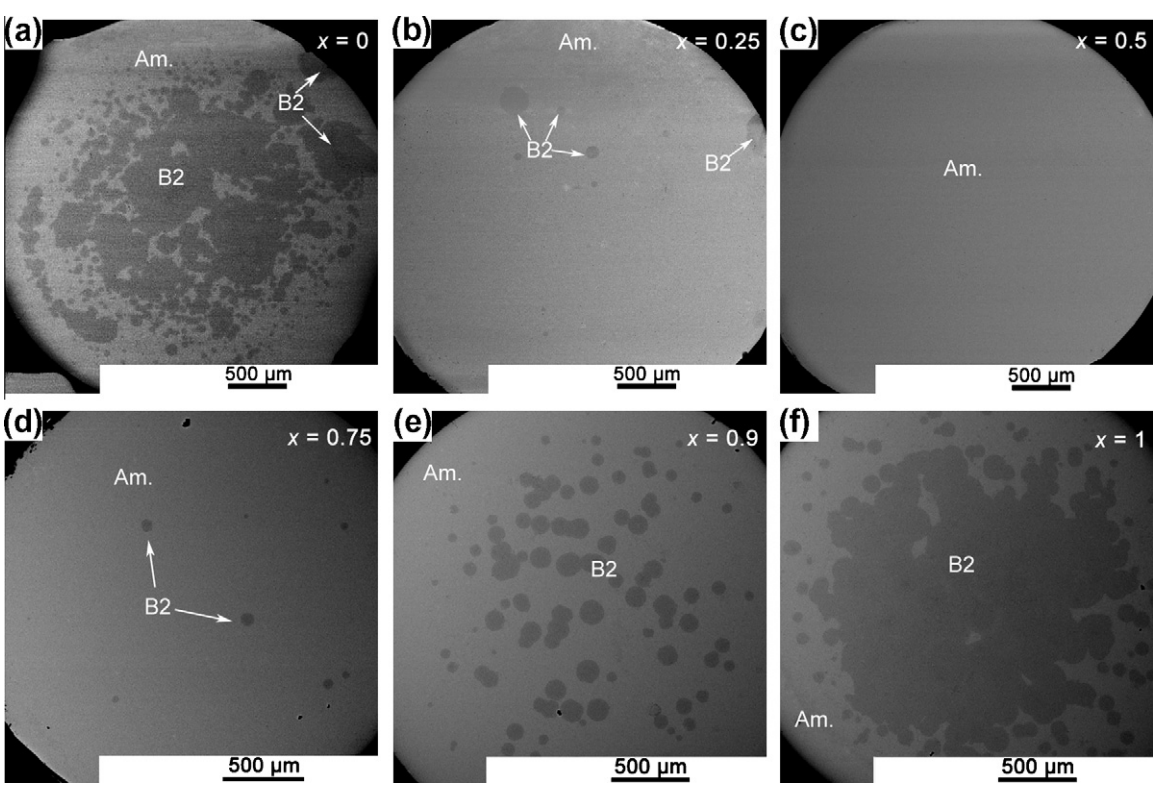

Fig. 2. SEM images of the transverse microstructures of the as-cast 3 mm diameter rods of the $Cu_{47}Zr_{48-x}Al_5Ta_x$ ($0 \leqslant x \leqslant 1$, at.%) alloys.

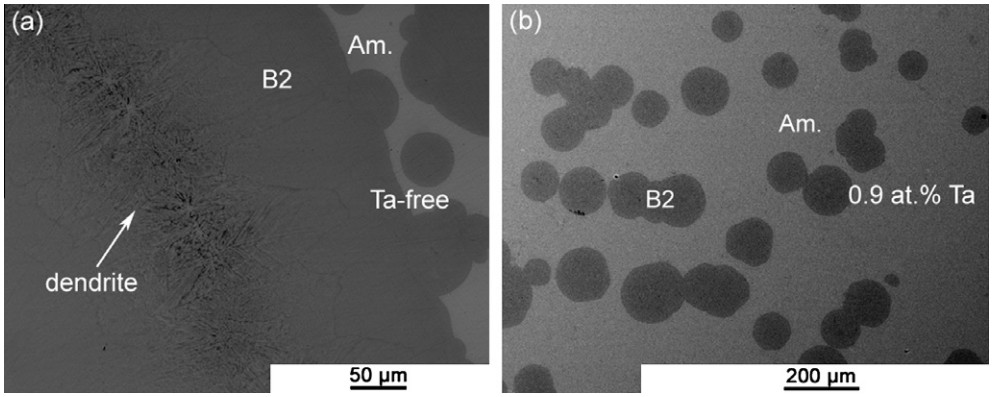

Fig. 3. Magnified SEM micrographs of the as-cast 3 mm diameter rods of Ta-free (a) and 0.9% Ta-added alloys (b).

fraction varies with Ta content from ~1% for the 0.75% Ta-added sample to ~10% for the 0.9% Ta-added sample. Even for the sample with 1% Ta addition, despite its high crystalline volume fraction (~55%), the B2 CuZr phase cannot be found at the surface and the sizes of individual particles not connected with other particles are more uniform than those in the Ta-free sample (Fig. 2f).

The homogenizing effect can be quantitatively illustrated by comparing the radial distribution of the B2 CuZr phase in the Ta-free and 0.9% Ta-added samples [46]. The cross-section of the 3 mm diameter rod was divided into 20 concentric rings along the radial direction and the volume fraction of the B2 CuZr phase in each ring was plotted vs. the radius of its centerline. Here only the micron-scale crystals detectable by SEM were included in the statistics. As shown in Fig. 4a, the crystalline volume fraction shows a sharp decrease radially from the center to the edge of the rod for the Ta-free samples, while the distribution of the particles in samples with 0.9% Ta addition can be seen to be more homogeneous. Fig. 4b shows the size distribution of particles in the Ta-free and 0.9% Ta-added samples obtained from more than 100 particles for each composition. The particles in the 0.9% Ta-added sample exhibit more uniform sizes compared with those in the Ta-free one, which ranged from ~10 μm to more than 500 μm. Therefore, the addition of 0.9% Ta plays an effective role in homogenizing the sizes and distribution of B2 CuZr particles in the present BMG composites.

3.2. Mechanical properties

To investigate the mechanical properties of the alloys with different Ta additions, compression tests were first performed on the 3 mm diameter specimens with an aspect ratio of 2:1. As shown in Fig. 5a, the samples exhibit characteristic compressive mechanical properties strongly dependent on their structures. The Ta-free sample, although with non-uniform sizes and distribution of B2 CuZr particles, shows prominent work-hardening ability and plasticity with a compressive strength of 1288 ± 52 MPa. With the decrease in crystalline volume

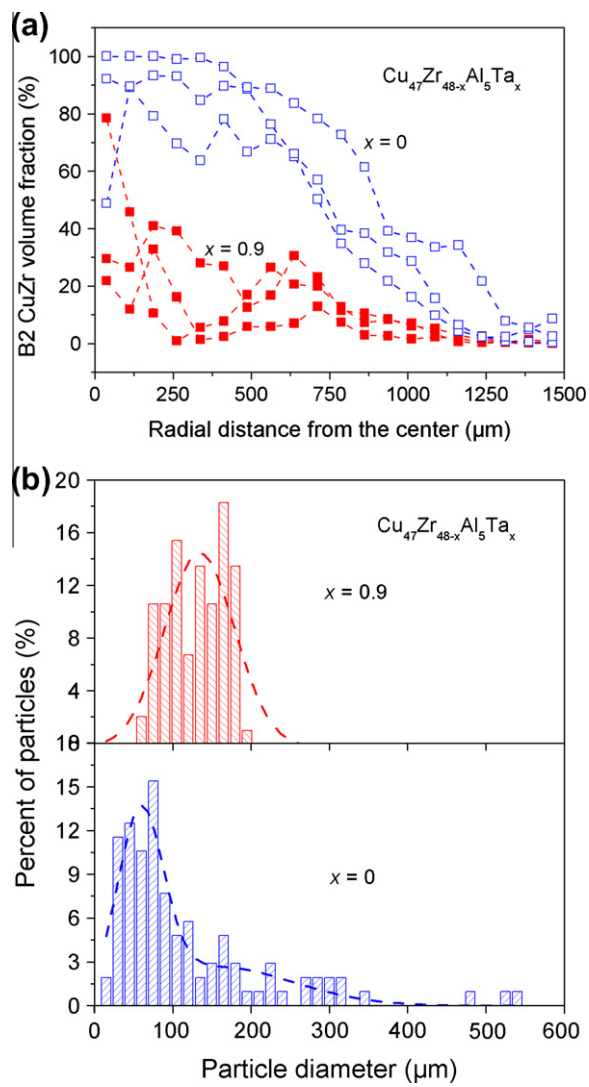

Fig. 4. Radial distributions (a) and size distributions (b) of the micron-scale B2 CuZr particles for the as-cast 3 mm diameter Ta-free and 0.9% Ta-added composites.

fractions the composites, like the 0.25% and 0.75% Ta samples, display increased strength but decreased plasticity, which agrees well with the trend reported by Pauly et al.

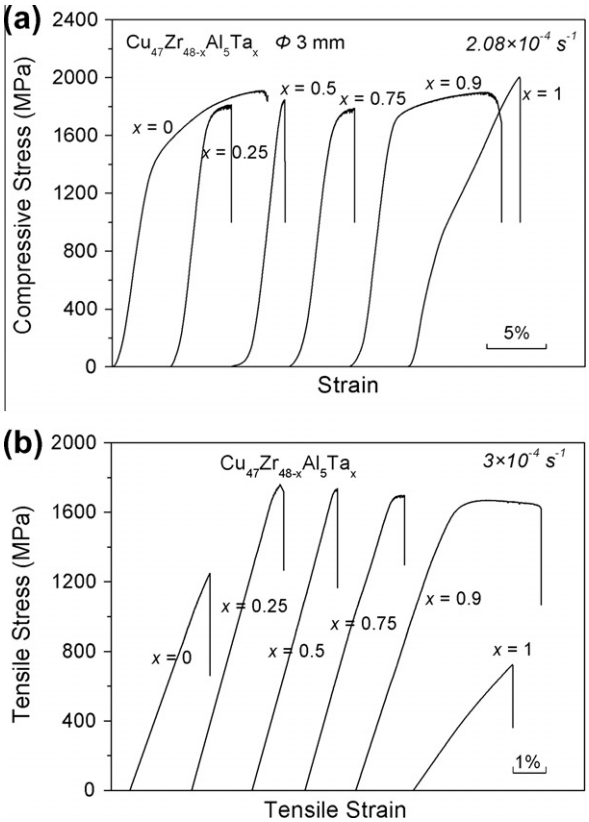

Fig. 5. Room temperature stress–strain curves for the as-cast samples with a diameter of 3 mm with different Ta additions under compression (a) and tension (b).

[28,29]. The sample with 0.5% Ta addition fractures catastrophically without detectable plasticity in accordance with its amorphous structure, while the compressive behavior of the 1% Ta-added sample is similar to that reported for the shape memory B2 CuZr crystal due to its high crystalline volume fraction [29]. Therefore, the volume fraction of the B2 CuZr phase can be regarded as a key factor governing the mechanical properties of the alloys under compression, consistent with the previously reported results [29]. However, microstructural homogenization is supposed to benefit the compressive properties of the composites, as can be seen by comparing the Ta-free and 0.9% Ta-added samples. The alloy with 0.9% Ta addition exhibits not only a much higher compressive strength of 1611 ± 68 MPa due to the lower crystalline volume fraction but also a pronounced work-hardening behavior and large compressive plasticity comparable to that in the Ta-free samples. The improved combination of mechanical properties ought to be attributed to the uniform sizes and homogeneous distribution of B2 CuZr particles in the composites [22].

The ductility of the alloys was further assessed by conducting tensile tests on the dog-bone-shaped samples machined from the as-cast 3 mm diameter rods. As shown in Fig. 5b, distinct yielding and large tensile ductility can only be achieved in the 0.9% Ta-added sample with crystalline particles homogeneously distributed within the glassy matrix. The 1% Ta-added alloy exhibits an obvious work-hardening behavior with slight ductility after yielding at a low strength of ~500 MPa, demonstrating the ductile nature of the crystalline phase [29,47]. For the Ta-free sample, however, premature fracture tends to occur without detectable yielding although the strength is higher than that of pure B2 CuZr crystals. The lack of ductility is attributed to the non-uniform particle sizes and heterogeneous distribution of the crystalline phase rather than the high crystallinity [22], because tensile ductility can be obtained even for the totally crystalline alloy as elucidated above. Therefore, the homogenization in sizes and distribution of B2 CuZr particles contributes not only to an improved combination of high strength and large plasticity under compression, but also to enhanced ductility in tension in the current composites. Furthermore, it should be noted that the composites exhibit "asymmetric" mechanical properties under compression and tension. The compressive mechanical properties depend mainly on the volume fractions of the B2 CuZr phase [29], while the tensile properties are strongly affected by the distribution of crystalline particles [22].

3.3. Fractographs of tensile samples

Fractography observations were conducted on the tensile fractured samples to understand the deformation and fracture mechanisms. The fracture occurs along a zig-zag path from the lateral view for the Ta-free sample without shear bands distinguishable on its lateral surface [48], as shown in Fig. 6a. As the interfaces between the crystalline phase and glassy matrix were reported to be the preferential crack nucleation sites due to stress concentration [21], particles with heterogeneous distribution (especially with crystals piling up in the center) and non-uniform sizes are not effective in inhibiting the propagation of cracks. In contrast, the sample with 1% Ta addition exhibits a plane fracture profile, which seems to be intergranular, as shown in Fig. 6b. Fig. 6c shows the lateral surface of a tensile fractured 0.9% Ta-added composite, revealing the formation of multiple shear bands. The propagation of shear bands is hindered by the crystalline particles embedded in the glassy matrix, resulting in the deflection and arrest of shear bands at the interface between the two phases. This blocking effect can be manifested by the shear bands ridged between two particles and the stagger of the scratch caused by polishing at the two-phase interface, indicated by white arrows in Fig. 6d. The applied strain can be accommodated by the formation of extensive shear bands as well as the multiplication and interaction of the bands, leading to prominent tensile ductility of the composite. Furthermore, cracks tend to propagate through the crystals rather than detour around the particles along separated interfaces, indicating a strong interface between the crystalline particles and glassy matrix in the composite, as shown in Fig. 6e. The crack changes its orientation when penetrating into crystals, as indicated by the arrows, and is arrested

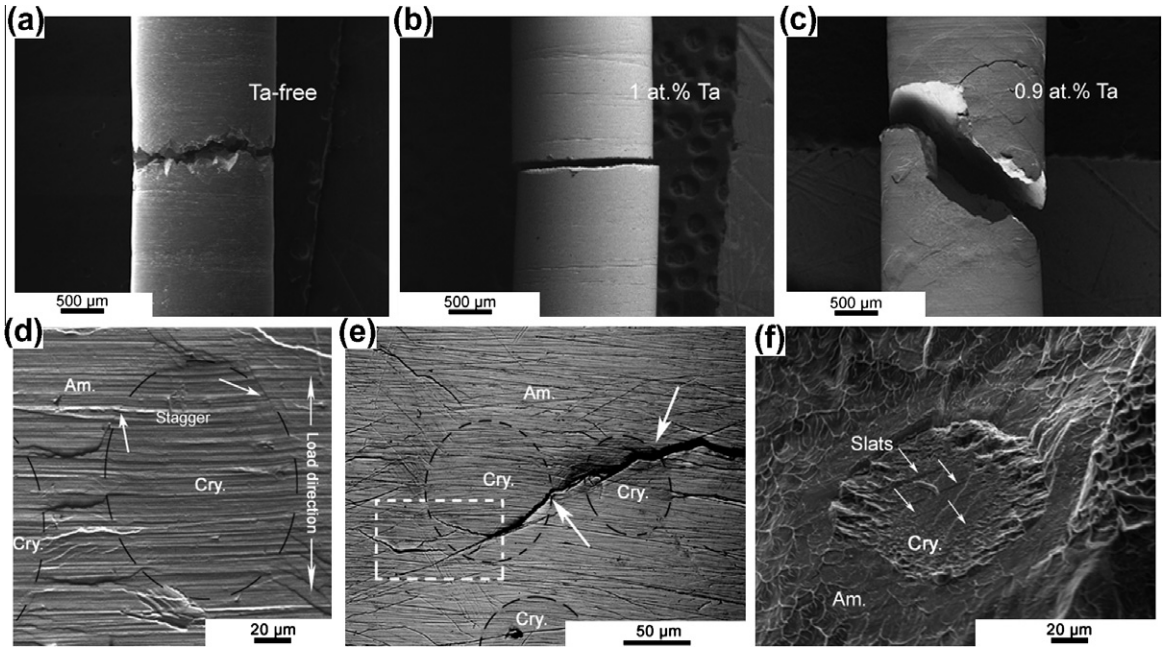

Fig. 6. SEM images of the lateral surfaces for the tensile fractured Ta-free (a) and 1 at.% Ta-added samples (b). Morphologies of the lateral surface for the tensile fractured 0.9% Ta-added sample are shown in (c–e) with a crack arrested by the microstructure (e). Figure (f) shows the image of a ruptured crystal embedded on the tensile fracture surface for the sample.

eventually after a hindered propagation along a characteristic wavy path. The strong interface can also be manifested by the ruptured crystalline particles embedded on the tensile fractured surface (Fig. 6f). Parallel slats typical of the lath martensite can be observed inside the particle as denoted by the white arrows, implying the existence of a martensite phase in the deformed sample.

4. Discussion

4.1. Mechanisms of the homogenizing effect

In order to explore the mechanisms underlying the homogenizing effect of Ta additions, the nucleation and growth kinetics of the 0.9% Ta-added and Ta-free samples were evaluated. Fig. 7a shows a high-resolution TEM image of the interface between a micron-scale crystalline particle and the glassy matrix for the 3 mm diameter sample with the selected diffraction patterns of each phase shown in the insets. The crystal is indexed as the B2 CuZr phase and the amorphous nature of the matrix is characterized by the diffuse halos, confirming the composite structure of the sample [21–32]. For the 1 mm diameter sample with a higher cooling rate, crystals in sizes of ~3 nm can be found precipitated in the glassy matrix, as indicated in Fig. 7b. With the decrease in cooling rate, the sizes of crystals increase to 78.2 ± 18.0 nm for the 1.5 mm diameter sample (Fig. 7c) and 89.2 ± 16.4 nm for the 2 mm diameter sample (Fig. 7d), respectively. The B2 CuZr structure of the crystals is identified by the diffraction patterns, as shown in the insets. In comparison, the as-cast 2 mm diameter sample of Ta-free alloy is proved to be fully amorphous without any crystalline nucleation by the featureless contrast in the high-resolution TEM image and broad diffraction halos illustrated in Fig. 7e. Therefore, it can be speculated that the nucleation of the B2 CuZr phase is promoted by 0.9% Ta addition during the rapid solidification process. Moreover, it should be noted that the facilitation in crystalline nucleation can only be found in the alloys with Ta contents above 0.5%. For the 0.5% Ta-added alloy with the optimal GFA, however, no crystalline phase is detected by TEM, even for the as-cast 3 mm diameter rod (Fig. 7f). This indicates that Ta additions up to ~0.5% dissolve absolutely in the alloys in the solute state. The promoted nucleation in the 0.9% Ta-added alloy is supposed to be induced by the superabundant Ta element over its solute limit.

Furthermore, the suppression on the growth of crystalline particles by Ta addition was validated by analyzing the growth kinetics in the 0.9% Ta-added and Ta-free alloys. As the cooling rate can be approximately determined as $\dot{T}(K \cdot s^{-1}) \approx 1000/R^2$ (mm) for a sample with a cast diameter of R [35], the relationship between the mean diameter of B2 CuZr particles d and the cooling rate $\dot{T}$ as well as the cast diameter R of the samples can be illustrated in Fig. 8. There exists a linear relationship between $\log d$ and $\log \dot{T}$. The dependence of grain size on the cooling rate during the rapid solidification can be expressed as:

$$\log d = A - n \log \dot{T}, \quad (1)$$

where A and n are constants. Eq. (1) can be further modified as:

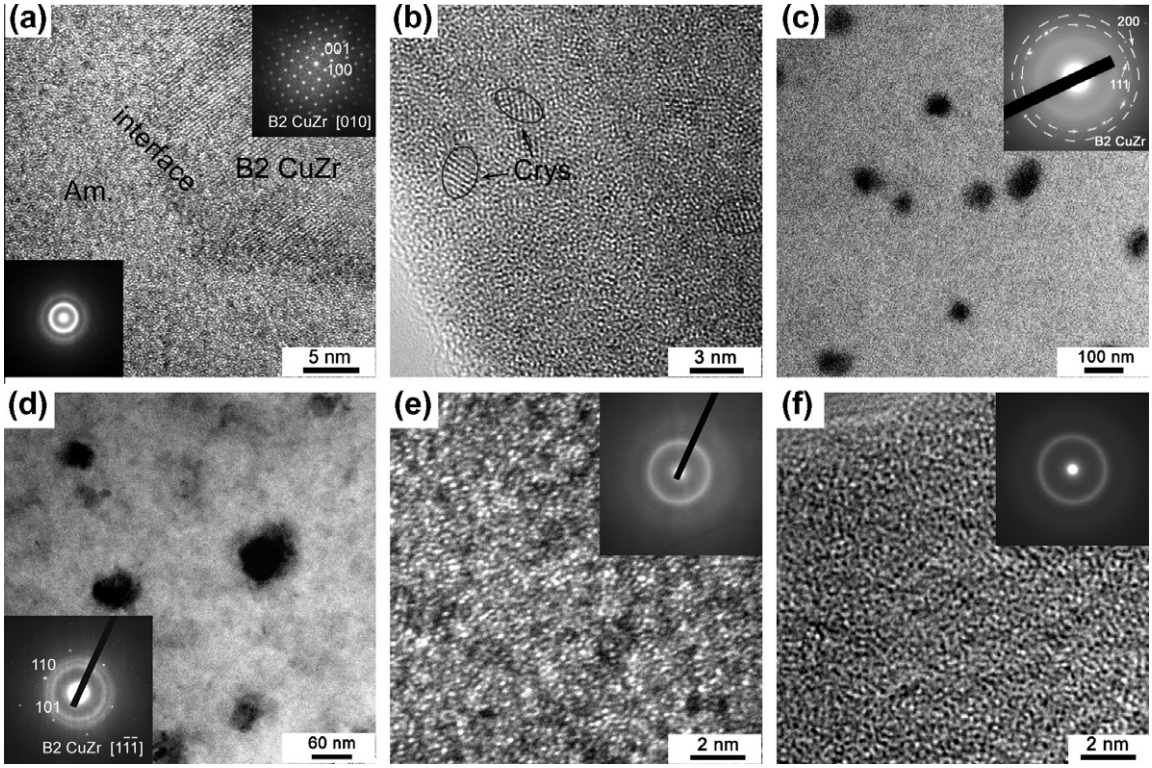

Fig. 7. High-resolution TEM image of the as-cast 3 mm diameter rod for the 0.9% Ta-added alloy with the electron diffraction patterns of the B2 CuZr phase and glassy matrix shown in the insets (a). Images of the as-cast rods with diameters of 1, 1.5, and 2 mm for the alloy are also presented in (b–d) with the crystalline structure identified by the diffraction patterns (insets). The amorphous nature of the as-cast 2 mm diameter rod for the Ta-free alloy (e) and 3 mm diameter rod for the 0.5% Ta-added alloy (f) are characterized by the high-resolution TEM images and corresponding diffraction patterns.

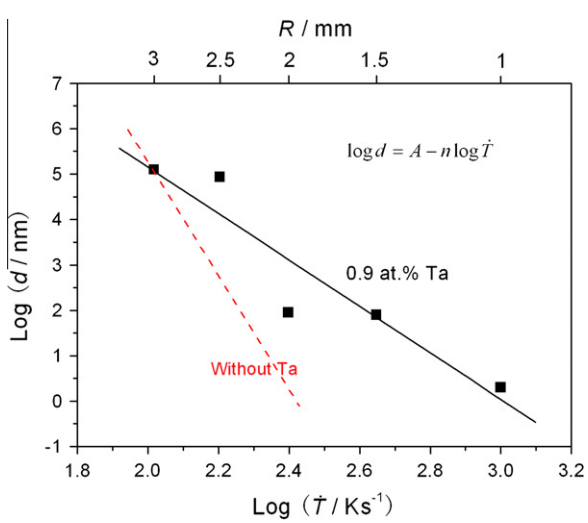

Fig. 8. Relationship between the mean diameter of crystalline particles d and the cooling rate $\dot{T}$ as well as the cast diameter R of the samples for the 0.9% Ta-added alloy. Result for the Ta-free sample is also shown for comparison.

$$d = B\dot{T}^{-n}, \tag{2}$$

where B and n are both constants. This agrees with the empirical relation reported for a wide variety of inorganic compounds [49–51]. A similar power relationship has also been reported for the cooling-rate dependence of mean grain size as well as the dendrite arm spacing for a series of crystalline alloys, despite the difference in cooling rates and glass-forming trend of the alloys [52–55]. The result for the Ta-free alloy is also illustrated in Fig. 8 for comparison. The suppressed growth of crystals in the 0.9% Ta-added alloy can be manifested by the decreased slope compared with the Ta-free sample. According to classical crystal growth theory [45,56,57], the growth velocity of the spherical crystal in the solidification process can be described as:

$$u = \frac{D}{a}\left[1 - \exp\left(-\frac{\Delta G}{kT}\right)\right], \tag{3}$$

where a is the interatomic spacing and k is Boltzmann's constant. Here ΔG denotes the difference in Gibbs free energy between the crystalline and liquid phases, T is the absolute temperature, and D denotes the effective diffusivity of atoms, respectively. Considering the same crystalline structure and temperature span for crystallization in the Ta-free and 0.9% Ta-added samples, the decreased growth rate is speculated to be attributed to the suppressed diffusivity of atoms.

Due to the atomic size mismatch between Ta and the base elements, a more efficient packing structure can be generated in the resulting alloy associated with the improvement of GFA with a proper minor Ta addition of up to ~0.5% primarily [58]. Thus the growth of B2 CuZr particles is supposed to be hindered due to the more

difficult rearrangement of atoms. The maximum solute Ta content is expected to be ~0.5% for glass formation in the matrix alloys based on the above results. The Ta content has exceeded this solute limit in the 0.9% Ta-added alloy. As a result, the superabundant Ta element, besides the solute state Ta, tends to precipitate from the alloys in the form of pure Ta or Ta-rich crystals in subnanometer scale sizes from the following three aspects. Firstly, the solid solubility of Ta in the base elements Cu, Zr and Al decreases significantly in the cooling process and eventually can be considered negligible at room temperature according to the binary phase diagrams [40]. Secondly, there exist positive heats of mixing between Ta and the main elements Cu and Zr, i.e. 2 kJ mol^{-1} for Ta–Cu and 3 kJ mol^{-1} for Ta–Zr pairs, and no intermetallic compounds can be formed between them [40,59]. In addition, Ta has a much higher melting point (~3300 K) than the matrix alloy (~1181 K) [40]. Owing to the same body-centered cubic (bcc) structure of the crystalline Ta and B2 CuZr phase with similar cell parameters ($a = 3.3058$ Å for Ta and 3.2562 Å for B2 CuZr), the precipitates may serve as potent nuclei for the nucleation of B2 CuZr particles, thus contributing to the uniform distribution of the particles [45,60–62]. The facilitation for nucleation of the B2 CuZr phase can be attributed to the superabundant Ta effect similar to that of inoculants in the inoculation operations widely adopted in the grain refinement of traditional crystalline alloys [45]. The microstructural evolution from the 0.75% to 1% Ta-added alloys is attributed to the difference in the amount of nuclei, i.e. the superabundant Ta contents in these alloys. Similar effect has been reported for Cu atoms in the FINEMET Fe–Si–B–Nb–Cu alloy, where pre-precipitated Cu clusters act as nucleation sites for the primary crystallization of the α-Fe phase [63,64].

Therefore, the nucleation of B2 CuZr crystals from the alloy melts is promoted and the growth is suppressed by 0.9% Ta addition in the alloys. This is supposed to account for the homogenization in sizes and distribution of B2 CuZr particles in the BMG composites. On one hand, B2 CuZr crystals nucleate more easily across the whole section of the rod during solidification, contributing to a good distribution of the crystalline particles. On the other hand, the rapid growth of individual crystals is hindered due to the sluggish growth kinetics. This is beneficial to avoid the overlapping of crystals, especially in the center of the cast rods where the cooling rate is lower.

4.2. Deformation and fracture mechanisms

The prominent tensile ductility of shape memory BMG composites has been attributed to the stress-induced martensitic transformation of the B2 CuZr phase during deformation [18–22,28–30]. In the present study, the occurrence of this transformation can be confirmed by the TEM observations on tensile fractured samples. As shown in Fig. 9a, typical morphology of the martensite phase can be observed in the crystals for the 0.9% Ta-added sample [22–24]. The B19′ structure of the crystalline phase is identified by the corresponding electron diffraction pattern shown in the inset. Not only are stress concentrations released by the energy-consuming transformation process, but the induced hardness increase in the crystals mitigates the strain-softening behavior of the glassy matrix [21,22,29]. In addition, although twinning was reported to be an important deformation mechanism in the martensite CuZr crystals [19,20,23], edge dislocations can also be detected in the crystals (Fig. 9b), revealing the presence of dislocation-mediated deformation mechanisms in the composite. The slipping, pinning, pile-up and interactions of dislocations in the crystalline phase are suspected to improve the ductility of the composite as in the crystalline alloys [65].

Correlations between the tensile fracture behaviors and the microstructural features can be understood by referring to the fracture mechanisms sketched in Fig. 10. In the Ta-free tensile sample that is taken from the central part of the rod, the B2 CuZr phase is the predominant one and can be regarded as the matrix phase; accordingly the amorphous is the second phase (Fig. 10a). However, the two phases are equally distributed and they surround each other. During tensile testing, the embedded harder amorphous phase has to bear additional high hydrostatic tensile stress due to their deformation discrepancy with the surrounding crystalline phase. The combining application of external tensile stress and hydrostatic tensile stress promotes the shearing and fracture of the amorphous phase, even in the macroscopic elastic deformation stage, inducing the nucleation of microcracks with variant orientations (Fig. 10a). The production of hydrostatic stress and the subsequent formation of microcracks are similar to what are observed and well known in metal composites reinforced with hard second-phase particles [66,67]. After their formation, the microcracks can either propagate or be arrested depending on whether or not the high energy/stress concentration ahead the microcrack tips will be effectively absorbed/relaxed by the surrounding phase. If the surrounding phase can be motivated to deform plastically or undergo phase transformation, the microcracks will be blunted and then arrested. However, the surrounding B2 CuZr phase in the present Ta-free sample has slight plastic deformation capability. Besides, the crystalline particles are too large in size, which makes the martensitic transformation difficult to achieve under the strong dimension constraint by their surrounding hard amorphous phase. Due to the lack of relaxation routes, the stress concentration ahead the microcrack tips will be further intensified with the increase in applied tensile stress. The ligament of the crystalline phase between neighboring microcracks will finally rupture under the intense stress concentration, coalescing the microcracks and causing full fracture of the sample. The variant orientations of the microcracks results in a zig-zag fracture angle from the lateral view, see Fig. 6a. But the sample has almost no tensile plastic strain, because the formation of extensive shear bands is remarkably

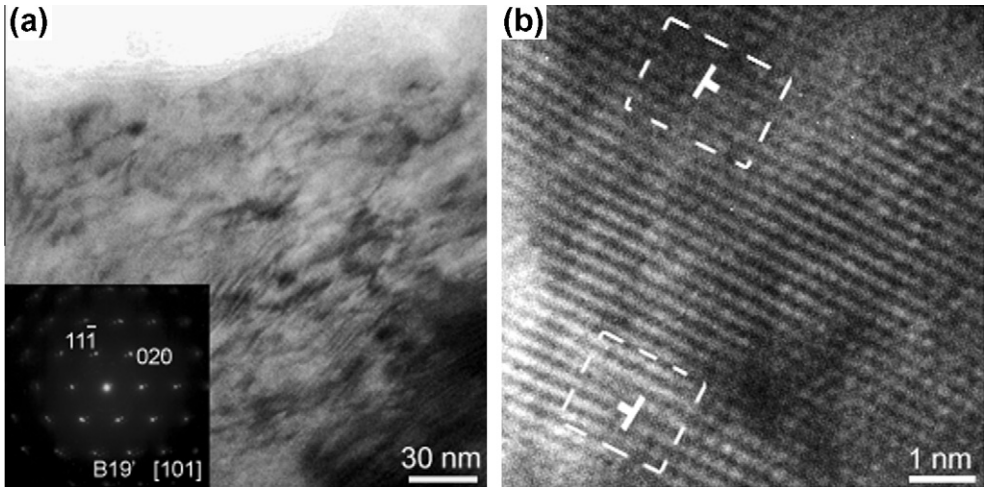

Fig. 9. TEM image of the martensite phase for the tensile fractured 0.9% Ta-added sample (a) with the corresponding electron diffraction pattern shown in the inset. Edge dislocations can be detected in the high-resolution TEM image of the crystalline phase (b).

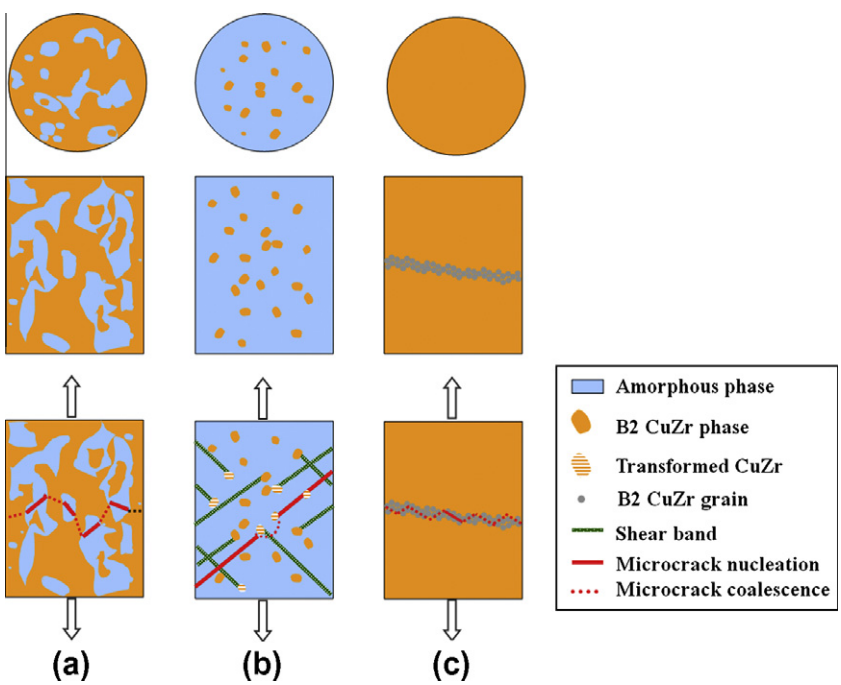

Fig. 10. Sketches illustrating the fracture mechanisms of Ta-free (a), 0.9% Ta-added (b), and 1% Ta-added (c) tensile samples, respectively. Note that the tensile samples are taken from the central part of the rods. Transverse images, longitudinal images before testing, and longitudinal images after testing are shown to demonstrate the effect of microstructures on the fracture behaviors. In (c), only several layers of CuZr grains are shown just to demonstrate the intergranular fracture.

suppressed in the embedded amorphous phase and the B2 CuZr phase is also accelerated to rupture by the concentrated stress conditions.

In comparison, the tensile fracture mechanism is quite different in the 0.9% Ta-added sample that has microstructural features distinct from those of its Ta-free counterpart. As shown in Fig. 10b, the matrix of the 0.9% Ta-added sample is the amorphous phase and the B2 CuZr particles, spherical in morphology and smaller in size, are homogeneously distributed in the matrix. The amorphous phase is no longer constrained by the B2 CuZr phase, which means that many more shear bands can be formed once the pre-existing shear bands have been blocked by the crystalline particles. In addition, the B2 CuZr particles with reduced size are liable to undergo martensitic transformation when impacted by shear bands, because the induced dimensional variations are relatively smaller and hence easier to accommodated via interactions with shear bands. As a result, some shear bands are effectively blocked by the particles through martensitic transformation to relax the high energy. More shear bands, including secondary ones, are subsequently induced. The formation of extensive shear

bands together with the phase transformation in CuZr particles are responsible for enhanced plastic deformation capability (~2.5%) in the 0.9% Ta-added sample (Fig. 10b). As to the 1% Ta-added alloy, the tensile sample is almost fully crystalline B2 CuZr. I-type microcracks are ready to form under applied tensile loading. These microcracks will propagate along the weak grain boundaries to cause the sample to rupture quickly (Fig. 10c). Intergranular fracture style can be clearly found on the fracture surface, which can be used to reasonably explain the low plastic strain of the 1% Ta-added tensile sample.

4.3. Modeling of the tensile plastic strain

In the following, the tensile plastic strain of the present BMG composites was modeled by different approaches through quantitatively describing the microstructures. Only the composites with Ta additions of 0.5, 0.75 and 0.9% were chosen for calculation, because the amorphous matrix of the three composites can be approximately considered to have the same composition or the same properties. Simple averaging analyses are firstly employed to estimate the plastic strain. In Case I (inset in the bottom right of Fig. 11a), one can assume that the composites are composed of amorphous matrix and pure B2 CuZr second phase in parallel configuration. The tensile plastic strain of the composites, ε_p^t, can be described by the rule-of-mixture:

$$\varepsilon_p^t = f_m \varepsilon_p^m + f_s \varepsilon_p^s, \tag{4}$$

where f and ε_p are the volume fraction and tensile plastic strain of the constituent phases, and the subscript/superscripts m and s refer to the BMG matrix and the B2 CuZr phase, respectively. Based on the experimental measurements on f and ε_p, ε_p^t is calculated using Eq. (4) and compared with the experimental results, as shown in Fig. 11a by open dots. It is clearly found that Eq. (4) underestimates ε_p^t unreasonably. The most possible reason for the underestimation is that the blocking effect of shear bands and the phase transformation of CuZr particles are not taken into account in Eq. (4) in the Case I consideration. A revision is thus made following the treatment of Fan and Miodownik who have developed an empirical approach to estimate the ductility of two-phase composites [68]. In this approach, the composites can be topologically transformed into a two-microstructural-element body. Typically illustrated in the top left inset in Fig. 11a (Case II), Element M consists only of the amorphous phase while Element C consists of both the B2 CuZr phase and the amorphous phase in equal content and the two phases are homogenously partitioned by each other to form an ideal inter-dispersed structure. Both the contributions of shear-band blocking and crystalline phase transformation can be simply considered in Element C, whose tensile plastic strain (ε_p^c) will be significantly improved by the contributors and their interactions. The tensile plastic strain of the composites is then given by the following equation:

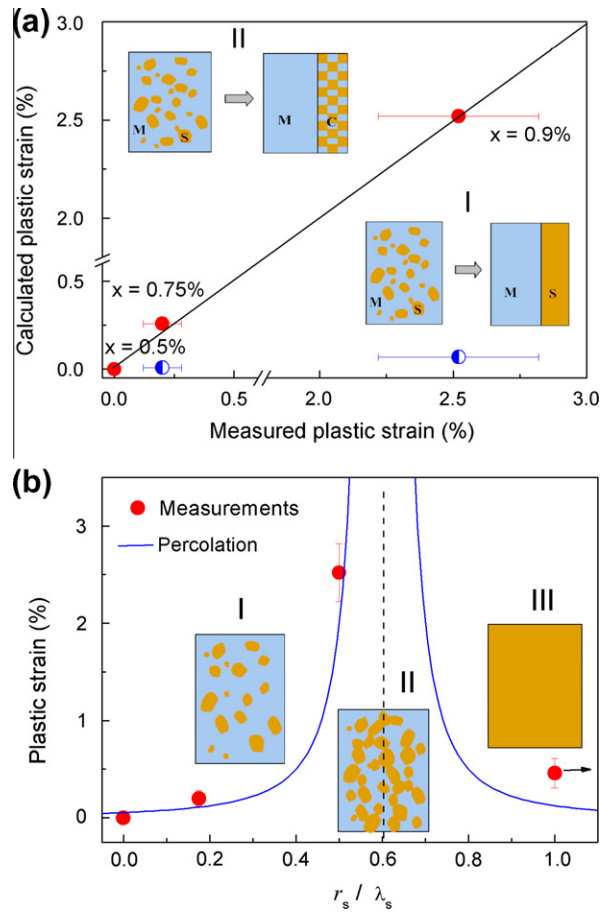

Fig. 11. (a) Experimentally measured tensile plastic strain (ε_p^t) vs. calculations by using simple averaging analyses for the composites with Ta addition of 0.5%, 0.75%, and 0.9%. Open dots and closed dots are corresponding to the microstructural configurations of Case I and Case II, respectively. (b) Dependence of ε_p^t on Γ or r_s/λ_s. Dots are experimental measurements and the solid line is from percolation theory. The dashed line indicates the percolation threshold $\Gamma_{cri} \sim 0.6$. The insets schematically show the representative microstructures of the composite with dilute B2 CuZr particles (inset I, $r_s/\lambda_s < 0.6$), of the composite with enough B2 CuZr particles to reach percolation threshold (inset II, $r_s/\lambda_s \approx 0.6$), and of the pure CuZr sample (inset III, $r_s/\lambda_s \to \infty$).

$$\varepsilon_p^t = f_m^c \varepsilon_p^m + f_c \varepsilon_p^c, \tag{5}$$

where the volume fraction of Element C, f_c, is two times f_s, and f_m^c is the corrected volume fraction of Element M as $f_m^c = f_m - f_s$, respectively. Taking $\varepsilon_p^c = 8\%$, the predictions by Eq. (5) are in good agreement with the experiments, as shown in Fig. 11a by closed dots. This indicates that in a simple way the topological microstructural-element treatment is applicable in describing the volume-weighted relationship between the microstructure and tensile plastic strain of the present composites.

In addition to the volume fractions of constituents, other key microstructural features of the particle-reinforced BMG composites also include the dimensional parameters of the second phase particles, such as particle size and inter-particle spacing. The variation in particle size and distribution is surely to cause the composite to exhibit

different deformation behavior and ductility. However, neither the particle radius (r_s) nor the spacing (λ_s) is involved in Eqs. (4) and (5). The tensile plastic strain will be further modeled by using the percolation theory, where both the parameters of r_s and λ_s are taken into account.

Recent experiments [69–71] revealed that, in the BMG composites reinforced with "ductile" second phase, the ductility will be suddenly increased at a topological transition in microstructure. The point of topological transition, called percolation threshold, is actually a statistical critical microstructural condition where the distribution of the second phase can effectively block all the shear bands emitted from different sites and in different orientations. Here, a combination of parameters, $\Gamma(=r_s/\lambda_s)$, rather than the volume fraction f_s is used to characterize the distribution feature of B2 CuZr particles. On the one hand, r_s/λ_s, the ratio of CuZr particle size to the ligament size, represents the possible percentage of blocked shear bands to a first approximation. On the other hand, r_s/λ_s is also directly related to f_s. For example, if the spherical particles are distributed in a cubic arrangement, $f_s \approx \frac{4}{3}\pi r_s^3/(\lambda_s + 2r_s)^3$. After defining Γ, the characteristic microstructural parameter, the tensile plastic strain of the composites can be written as a function of Γ by referring to traditional expressions for the percolation theory [72]:

$$\varepsilon_p^t \propto (\Gamma_{cri} - \Gamma)^{-v}, \text{ or } \varepsilon_p^t = \varepsilon_p^0(\Gamma_{cri} - \Gamma)^{-v} \quad (6)$$

where Γ_{cri} is the percolation threshold or the critical point of Γ, v is the exponent and ε_p^0 is a constant. Fitting Eq. (6) to experimental results (see Fig. 11b), the percolation threshold Γ_{cri} and exponent v are determined as 0.6 and 2, respectively. It is revealed from Fig. 11b that the sudden increase in ε_p^c is experimentally observed at Γ (or r_s/λ_s) ~ 0.5 in the 0.9% Ta-added sample, which is in the vicinity of the percolation threshold of 0.6. This indicates that the percolation theory can be used to reasonably explain the present experimental results and well describe the tensile plastic strain with respect to the characteristic microstructural parameter of r_s/λ_s.

Therefore, the present strategy is quite effective in homogenizing the sizes and distribution of the B2 CuZr phase, thus improving the mechanical properties of BMG composites. The basic principles followed here, i.e. facilitating the nucleation from an aspect of inoculation and suppressing the growth of crystalline particles, have been proved to be applicable to other alloying elements, such as W (results not shown here). In addition, the microstructural element body approach and perculation theory, which give good explanations for the tensile ductility of current composites, are expected to give implications for the structural design of the series of BMG composites.

5. Conclusions

Effects of Ta additions on the microstructures and mechanical properties of rapidly solidified $Cu_{47}Zr_{48-x}Al_5Ta_x$ ($0 \leqslant x \leqslant 1$, at.%) alloys were investigated systematically, and BMG composites with the B2 CuZr phase precipitated within the glassy matrix were obtained by suitably adjusting the Ta contents. The sizes and distribution of crystalline particles were effectively homogenized by 0.9% Ta addition. It was proved that the microstructural homogenization is beneficial not only to improved combination of high strength and large plasticity under compression, but also to enhanced ductility in tension for the composites. This homogenizing effect was attributed to the facilitation in nucleation and suppression in growth of the crystals by investigating the cooling-rate dependence of crystal sizes. The prominent tensile property was attributed to deformation-induced martensitic transformation of the crystalline phase as well as the blocking effect for the propagation of shear bands and cracks by the ductile crystalline phase and strong two-phase interfaces. Fracture mechanisms of the alloys were analyzed and correlated with the microstructures of the alloys. Tensile plastic strain was also quantitatively modeled by using an empirical microstructural element body approach as well as percolation theory, which both gave reasonable explanations for the experimental results. This study provides a strategy in optimizing the microstructures of BMG composites and has important implications for the development and applications of the composites.

Acknowledgements

This work was supported by the National Basic Research Program of China (Grant Nos. 2007CB613900 and 2010CB631003), the Natural Science Foundation of China (Grant Nos. 51071008 and 51131002), the Innovation Foundation of BUAA for PhD Graduates, and Program for New Century Excellent Talents in University (NCET).

References

[1] Inoue A, Zhang T, Masumoto T. Mater Trans JIM 1990;31:177.
[2] Peker A, Johnson WL. Appl Phys Lett 1993;63:2342.
[3] Inoue A. Acta Mater 2000;48:279.
[4] Liu ZQ, Li R, Wang G, Wu SJ, Lu XY, Zhang T. Acta Mater 2011;59:7416.
[5] Ashby MF, Greer AL. Scripta Mater 2006;54:321.
[6] Yavari AR, Lewandowski JJ, Eckert J. MRS Bull 2007;32:635.
[7] Schuh CA, Hufnagel TC, Ramamurty U. Acta Mater 2007;55:4067.
[8] Choi-Yim H, Johnson WL. Appl Phys Lett 1997;71:3808.
[9] Hays CC, Kim CP, Johnson WL. Phys Rev Lett 2000;84:2901.
[10] Eckert J, Kühn U, Mattern N, He G, Gebert A. Intermetallics 2002;10:1183.
[11] Park ES, Kim DH. Met Mater Int 2005;11:19.
[12] Eckert J, Das J, Pauly S, Duhamel C. J Mater Res 2007;22:285.
[13] Li Y, Poon SJ, Shiflet GJ, Xu J, Kim DH, Löffler JF. MRS Bull 2007;32:624.
[14] Wu FF, Zhang ZF, Mao SX, Peker A, Eckert J. Phys Rev B 2007;75:134201.
[15] Hoffmann DC, Suh JY, Wiest A, Duan G, Lind ML, Demetriou MD, et al. Nature 2008;451:1085.

[16] Park JM, Jayaraj J, Kim DH, Mattern N, Wang G, Eckert J. Intermetallics 2010;18:1908.
[17] Schramm JP, Hofmann DC, Demetriou MD, Johnson WL. Appl Phys Lett 2010;97:241910.
[18] Hofmann DC. Science 2010;329:1294.
[19] Pauly S, Gorantla S, Wang G, Kühn U, Eckert J. Nat Mater 2010;9:473.
[20] Pauly S, Liu G, Gorantla S, Wang G, Kühn U, Kim DH, et al. Acta Mater 2010;58:4883.
[21] Wu Y, Xiao YH, Chen GL, Liu CT, Lu ZP. Adv Mater 2010;22:2770.
[22] Wu Y, Wang H, Wu HH, Zhang ZY, Hui XD, Chen GL, et al. Acta Mater 2011;59:2928.
[23] Sun YF, Wei BC, Wang YR, Li WH, Cheung TL, Shek CH. Appl Phys Lett 2005;87:051905.
[24] Jiang F, Zhang ZB, He L, Sun J, Zhang H, Zhang ZF. J Mater Res 2006;21:2638.
[25] Pauly S, Das J, Duhamel C, Eckert J. Adv Eng Mater 2007;9:487.
[26] Eckert J, Pauly S, Das J, Duhamel C. Adv Eng Mater 2007;9:443.
[27] Zhang LC, Jiang F, Zhang DH, He L, Sun J, Fan JT, et al. Adv Eng Mater 2008;10:943.
[28] Pauly S, Liu G, Wang G, Das J, Kim KB, Kühn U, et al. Appl Phys Lett 2009;95:101906.
[29] Pauly S, Liu G, Wang G, Kühn U, Mattern N, Eckert J. Acta Mater 2009;57:5445.
[30] Pauly S, Das J, Bednarcik J, Mattern N, Kim KB, Kim DH, et al. Scripta Mater 2009;60:431.
[31] Wei XF, Sun YF, Guan SK, Terada D, Shek CH. Mater Sci Eng A 2009;517:375.
[32] Das J, Pauly S, Boström M, Durst K, Göken M, Eckert J. J Alloys Compd 2009;483:97.
[33] Song KK, Pauly S, Zhang Y, Gargarella P, Li R, Barekar NS, et al. Acta Mater 2011;59:6620.
[34] Clyne TW, Withers PJ. An introduction to metal matrix composites. Cambridge: Cambridge University Press; 1993.
[35] Lin XH, Johnson WL. J Appl Phys 1995;78:6514.
[36] Tan H, Zhang Y, Li Y. Intermetallics 2002;10:1203.
[37] Hu X, Ng SC, Feng YP, Li Y. Acta Mater 2003;22:561.
[38] Kumar G, Desai A, Schroers J. Adv Mater 2011;33:461.
[39] Huang YJ, Shen J, Sun JF. Appl Phys Lett 2007;90:081919.
[40] Massalski TB, Okamoto H, Subramaniam PR, Kacprzak L. Binary alloy phase diagrams. 2nd ed. Materials Park (OH): ASM International; 1990.
[41] Liu Y, Liu CT, George EP, Wang XZ. Appl Phys Lett 2006;89:051919.
[42] Liu Y, Liu CT, George EP, Wang XZ. Intermetallics 2007;15:557.
[43] Liu ZQ, Li R, Wang H, Zhang T. J Alloys Compd 2011;509:5033.
[44] Liu ZQ, Li R, Huang L, Lu XY, Zhang T. J Non-Cryst Solids 2011;357:3190.
[45] Biloni H, Boettinger WJ. In: Cahn RW, Haasen P, editors. Physical metallurgy. Amsterdam: Elsevier; 1996.
[46] Han W, Eckschlager A, Bohm HJ. Compos Sci Technol 2001;61:1581.
[47] Sutrakar VK, Mahapatra DR. Intermetallics 2010;18:679.
[48] Thomson RL. In: Cahn RW, Haasen P, editors. Physical metallurgy. Amsterdam: Elsevier; 1996.
[49] Cashman KV. Contrib Mineral Petrol 1993;113:126.
[50] Ikeda Y, Can J. Earth Sci 1977;14:1860.
[51] Grove TL, Walker D. Proc Lunar Planet Sci Cont 8th 1977:1501.
[52] Jones H. J Mater Sci 1984;19:1043.
[53] Boswell PG, Chadwick GA. Scripta Metall 1977;11:459.
[54] Greer AL, Bunn AM, Tronche A, Evans PV, Bristow DJ. Acta Mater 2000;48:2823.
[55] Greer AL. Phil Trans Roy Soc Lond A 2003;361:479.
[56] Schroers J, Johnson WL. J Appl Phys 2000;88:44.
[57] Schroers J, Johnson WL, Busch R. Appl Phys Lett 2000;76:2343.
[58] Clementi E, Raimondi DL, Reinhardt WT. J Chem Phys 1967;47:1300.
[59] De Boer FR, Room R, Mattens WCM, Miedema AR, Niessen AK. Cohesion in metals. Amsterdam: North-Holland; 1989.
[60] Zhalko-Titarenko AV, Yevlashina ML, Antonov VN, Yavorskii BY, Koval YN, Firstov GS. Phys Status Solidi B 1994;184:121.
[61] Swanson HE, Tatge E. Natl Bur Stand (US) Circ 1953;539:129.
[62] Xu WQ, Zheng RK, Laws KJ, Ringer SP, Ferry M. Acta Mater 2011;59:7776.
[63] Hono K, Li JL, Ueki Y, Inoue A, Sakurai T. Appl Surf Sci 1993;67:398.
[64] Hono K, Ping DH, Ohnuma M, Onodera H. Acta Mater 1999;47:997.
[65] Hirth JP. In: Cahn RW, Haasen P, editors. Physical metallurgy. Amsterdam: Elsevier; 1996.
[66] Goods SH, Brown LM. Acta Mater 1979;27:1.
[67] Liu G, Sun J, Nan CW, Chen KH. Acta Mater 2005;53:3459.
[68] Fan Z, Miodownik AP. Scripta Metall Mater 1993;28:895.
[69] Lee ML, Li Y, Schuh CA. Acta Mater 2004;52:4121.
[70] Fu XL, Li Y, Schuh CA. Acta Mater 2007;55:3059.
[71] Fu XL, Li Y, Schuh CA. Scripta Mater 2007;56:617.
[72] Nan CW. Prog Mater Sci 1993;37:1.